Citation for published version:
Chen, Q, Zang, J, Birchall, J, Ning, DZ, Zhao, X & Gao, J 2020, 'On the hydrodynamic performance of a vertical pile-restrained WEC-type floating breakwater', *Renewable Energy*, vol. 146, pp. 414-425. https://doi.org/10.1016/j.renene.2019.06.149

DOI:
10.1016/j.renene.2019.06.149

Publication date:
2020

Document Version
Peer reviewed version

Link to publication

On the hydrodynamic performance of a vertical pile-restrained WEC-type floating breakwater

Qiang Chen[a,b], Jun Zang[a,b,*], Jonathan Birchall[a], Dezhi Ning[b], Xuanlie Zhao[b], Junliang Gao[c]

[a] *Research Unit for Water, Environment and Infrastructure Resilience (WEIR), Department of Architecture and Civil Engineering, University of Bath, BA2 7AY, U.K.*
[b] *State Key Laboratory of Coastal and Offshore Engineering, Dalian University of Technology, Dalian, 116024, China*
[c] *School of Naval Architecture and Ocean Engineering, Jiangsu University of Science and Technology, Zhenjiang, 212003, China*

Abstract

This paper presents a numerical study on the hydrodynamic performance of a vertical pile-restrained wave energy converter type floating breakwater. The aims are to further understand the characteristics of such integrated system in terms of both wave energy extraction and wave attenuation, and to provide guidance for optimising the shape of the floating breakwater for more energy absorption and less wave transmission at the same time. The numerical model solves the incompressible Navier-Stokes equations for free-surface flows using the particle-in-cell method and incorporates a Cartesian cut cell based strong coupling algorithm for fluid-structure interaction. The numerical model is first validated against an existing experiment, consisting of a rectangular box as the floating breakwater and a power take-off system installed above the breakwater, for the computation of the capture width ratio and wave transmission coefficients. Following that, an optimisation study based on the numerical model is conducted focusing on modifying the shape of the floating breakwater used in the experiment. The results indicate that by changing only the seaward side straight corner of the rectangular box to a small curve corner, the integrated system achieves significantly more wave energy extraction at the cost of only a slight increase in wave transmission.

Keywords: Wave energy converters, Floating breakwater, Particle-In-Cell method, CFD

---

[*] Corresponding author.
Email address: `j.zang@bath.ac.uk` (Jun Zang)

Preprint submitted to Renewable Energy *May 24, 2019*

1. Introduction

For coastal areas with high tidal range and/or large water depth, floating breakwaters are frequently used as wave-attenuation structures, due to a number of advantages such as low environmental impact and flexibility [1]. Floating breakwaters with rectangular cross-sections, typically termed as box-type floating breakwaters [1], are widely adopted as they are simple, durable and cost-effective. Meanwhile, in the wave energy field, wave energy converters (WECs) of various types such as oscillating buoys, floating ducks and enclosed chambers have been investigated; nevertheless, cost reduction still remains a big challenge and requires advances [2]. It is found that the box-type floating breakwaters are similar to the oscillating buoy WECs in many aspects such as working conditions, structural characteristics and applied functions. Thus, the idea of integrating WECs into floating breakwaters provides a promising way to realize cost-sharing in wave energy technology [3]. The major concerns with respect to such integrated system include both the performance of wave attenuation and efficiency of power output. A number of pioneering studies show that it is possible to simultaneously realize the function of wave energy utilisation and desired-level wave attenuation for such integrated systems [4, 5, 6].

Ning et al. [6] experimentally studied the system of a vertical pile-restrained floating breakwater that is working under the principle of an oscillating buoy WEC. The integrated system comprises a rectangular box-type floating breakwater as base structure, with a power take-off (PTO) system installed above the breakwater without changing the geometry of the breakwater. Fig. 1 shows a schematic demonstrating the working principle of the integrated system. That is, the kinetic energy of the heave motion of the floating breakwater is captured by the above PTO system through mechanic transmission. The PTO damping force in turn affects the heave motion of the floating breakwater and hence the wave transmission coefficient. Their experimental results show that with the proper adjustment of PTO damping force, a range can be observed for which the capture width ratio (CWR, the ratio of captured energy and incident wave energy) of the system can achieve approximately 24%, with the transmission coefficient being lower than 0.50.

In this paper, the experimental setup used in Ning et al. [6] has been numerically studied using a Particle-In-Cell (PIC) method based model. The aims are to first validate the numerical model for simulating the performance of such WEC-type floating breakwater, and then apply the numerical model to a further optimisation study of the integrated system. It is understood that the rectangular box-type floating breakwater can lead to strong eddy making damping due to the straight corners and therefore small heave motion and hence

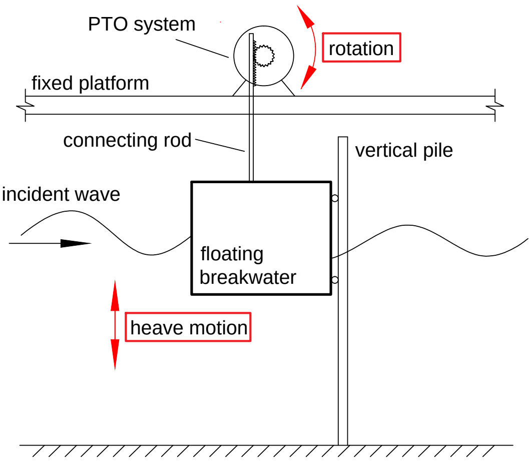

Fig. 1: Sketch (side view) of the integrated system.

low efficiency of wave energy transfer. On the other hand, because in the current system the floating breakwater has only heave motion, the straight corners can result in large wave reflection and therefore desired low wave transmission. Thus, the shape of the floating breakwater could be one of the predominant factors to the success of such integrated system. In the present work, the focus is on modifying the straight corners of the rectangular box-type floating breakwater to curve corners in order to reduce the eddy making damping due to wave-structure interaction. We show that by using the curve corner with a proper size and position, the motion of the floating breakwater can be increased significantly (and hence larger CWR coefficient), while the wave transmission coefficient is still kept within an acceptable level.

The numerical model used in the present study employs the hybrid Eulerian-Lagrangian PIC method to solve the incompressible Navier-Stokes equations (NSE) for single-phase free-surface flows, and incorporates a Cartesian cut cell based two-way strong coupling algorithm for fluid-structure interaction. The model is capable of simulating complex water-wave scenarios involving large free-surface deformations and the interaction of such flow with surface-piercing floating bodies of arbitrary configuration and degree of freedom. Moreover, as a Navier-Stokes solver, the viscous effects such as the eddy making damping are automatically accounted for. The PIC method dates back to 1950s [7, 8], and was devised with an aim to tackle the disadvantages of traditional Eulerian and Lagrangian methods [9]. The idea was to combine the uses of an Eulerian grid and a set of Lagrangian particles. In particular, the particles are used to solve any transport terms and track the fluid configuration such that sharp features of material interfaces can be captured, while the Eulerian grid is employed to solve the rest non-advection terms with computational robustness and efficiency. The early versions of the PIC method was successful but had many restrictions and difficulties, such as the large amount of particles required (hence large computing memory storage), relatively large numerical dissipation and low order of accuracy. Further developments can be found in, for example, Brackbill and Ruppel [10] and Brackbill et al. [11], which significantly reduce the numerical dissipation of PIC method. Recently, variations of the PIC method have achieved high-order accuracy (see Edwards and Bridson [12], Maljaars et al. [13] and Wang and Kelly [14]).

The PIC method has not attracted sufficient attention from the coastal and offshore engineering community until very recently. Kelly [15] initially proposed a PIC model for simulating solitary wave propagating onto a slop beach in two spatial dimensions (2D). Then, Kelly et al. [16] applied a PIC model augmented with a distributed Lagrange multiplier (DLM) method to handle problems that involve full two-way fluid-solid coupling. Later, Chen et al. [17] proposed a Cartesian cut cell based two-way strong fluid-solid coupling algorithm within their two-dimensional PIC model, which was further extended by Chen et al. [18] to three spatial dimensions with domain decomposition based massage passing interface (MPI) parallelisation. These studies have shown that the PIC method has great potential to become a high-quality CFD tool for use in coastal and offshore engineering applications. In fact, the PIC model used in this study is developed based on that proposed in Chen et al. [17]. We show that this PIC model can satisfactorily capture the key physical processes occurring in the scenario of wave interaction with a WEC-type floating breakwater.

The paper is organised as follows: Section 2 gives an overview of the current PIC model including the governing equations and major numerical implementations. Next, in Section 3 the numerical model is first validated for simulating wave interaction with the integrated system of WEC-type floating breakwater using the experiment proposed in Ning et al. [6], and then an optimisation study based on the numerical model is conducted focusing on modifying the shape of the floating breakwater in the experiment. Finally, in Section 4 conclusions are drawn.

2. Numerical Model

2.1. Governing equations

The current PIC model solves the incompressible Newtonian Navier-Stokes equations for single-phase flow, and incorporates a Cartesian cut cell based two-way strong fluid-solid coupling algorithm for fluid-structure interaction. The governing equations are:

$$\nabla\cdot \boldsymbol{u} \;=\; 0, \tag{1}$$

$$\frac{\partial \boldsymbol{u}}{\partial t} + (\boldsymbol{u}\cdot\nabla)\boldsymbol{u} = \boldsymbol{f} - \frac{1}{\rho}\nabla p + \nu\nabla^2\boldsymbol{u}, \tag{2}$$

with the following boundary conditions applied on the free surface and the freely moving structure surface:

$$p = 0 \quad \text{on } \zeta(\boldsymbol{x}, t), \tag{3}$$

where $\zeta(\boldsymbol{x}, t)$ represents the free-surface position and

$$\boldsymbol{u} = \boldsymbol{U}_b \quad \text{and} \quad \boldsymbol{n}\cdot(\Delta t\rho^{-1}\nabla p) = \boldsymbol{n}\cdot(\tilde{\boldsymbol{U}}_b - \boldsymbol{U}_b^{n+1}) \quad \text{on } \partial\Omega_S(\boldsymbol{x}, t), \tag{4}$$

where $\partial\Omega_S$ represents the structure surface. In 2D, $\boldsymbol{u} = [u, w]^T$ is the velocity field, p is pressure, t is time, $\boldsymbol{f} = [0.0,\ \text{-}9.81\ \text{m/s}^2]^T$ represents the body force due to gravity, and ν and ρ are the kinematic viscosity and density of the fluid respectively. In Eq. 4, $\tilde{\boldsymbol{U}}_b$ denotes a tentative velocity on the structure surface between $\boldsymbol{U}_b^n$ and $\boldsymbol{U}_b^{n+1}$, which represent the velocities on the structure surface at time steps n and $n+1$ respectively, and $\boldsymbol{n}$ is the unit outward normal vector of the structure surface. For full details of the equations solved in the current PIC model, the reader is referred to Chen et al. [17] and Chen [19].

2.2. Numerical solution procedure

The current PIC model employs the full particle PIC methodology following Brackbill and Ruppel [10]. The whole computational domain is discretised by a staggered Eulerian grid, and the fluid area is accommodated by a set of Lagrangian particles. Fig. 2 shows a schematic of the computational setup. To reduce numerical dissipation, all the fluid properties such as the mass and momentum are carried by the particles. At the beginning of each computational cycle, the velocity field carried by the particles is mapped onto the grid using a kernel interpolation that conserves the mass and momentum (see Chen et al. [18]). The free-surface position is also reconstructed on the grid based on the particle location. Then, the governing equations ignoring the advection term are solved on the grid using a pressure projection method proposed in Chorin [20]. During this stage, a pressure Poisson equation (PPE) is constructed and solved in a finite volume sense involving all the boundary conditions. Particularly, the Cartesian cut cell method based two-way strong fluid-solid coupling algorithm is employed to resolve the boundary conditions applied on the structure surface. Once this is done, a divergence-free velocity field and an acceleration field (i.e. velocity change) are obtained on the grid, which are then used to update the velocity field carried by the particles. Finally, the particles are moved to solve the remaining advection term and update the fluid configuration. Fig. 3 shows a general algorithm of the PIC model, where the changes of the main variables following each step are also given. As the Lagrangian particles are used to track the free surface, sharp features as well as large deformations of the fluid interface can be well captured; meanwhile, the employment of an Eulerian grid makes the model both efficient and robust when handling complex free-surface flow problems. Equally importantly, the aforementioned fluid-solid interaction scheme enables the model to simulate freely moving structures of arbitrary shape and degree of freedom. For full detail of the current PIC model, the interested reader is referred to Chen et al. [17] and Chen [19].

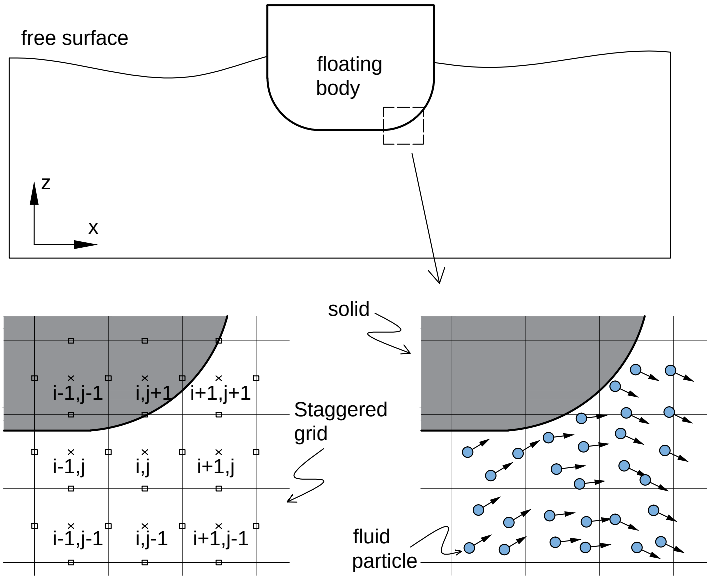

Fig. 2: Sketch of the computational domain, the staggered grid and fluid particles.

3. Model validation and optimisation study

In this section, the experiment of a vertical pile-restrained WEC-type floating breakwater presented in Ning et al. [6] is first used to validate the present PIC model. After that, an optimisation study based on the numerical model is conducted to further exploit the potential of the integrated system in the experiment. This is via changing the shape the

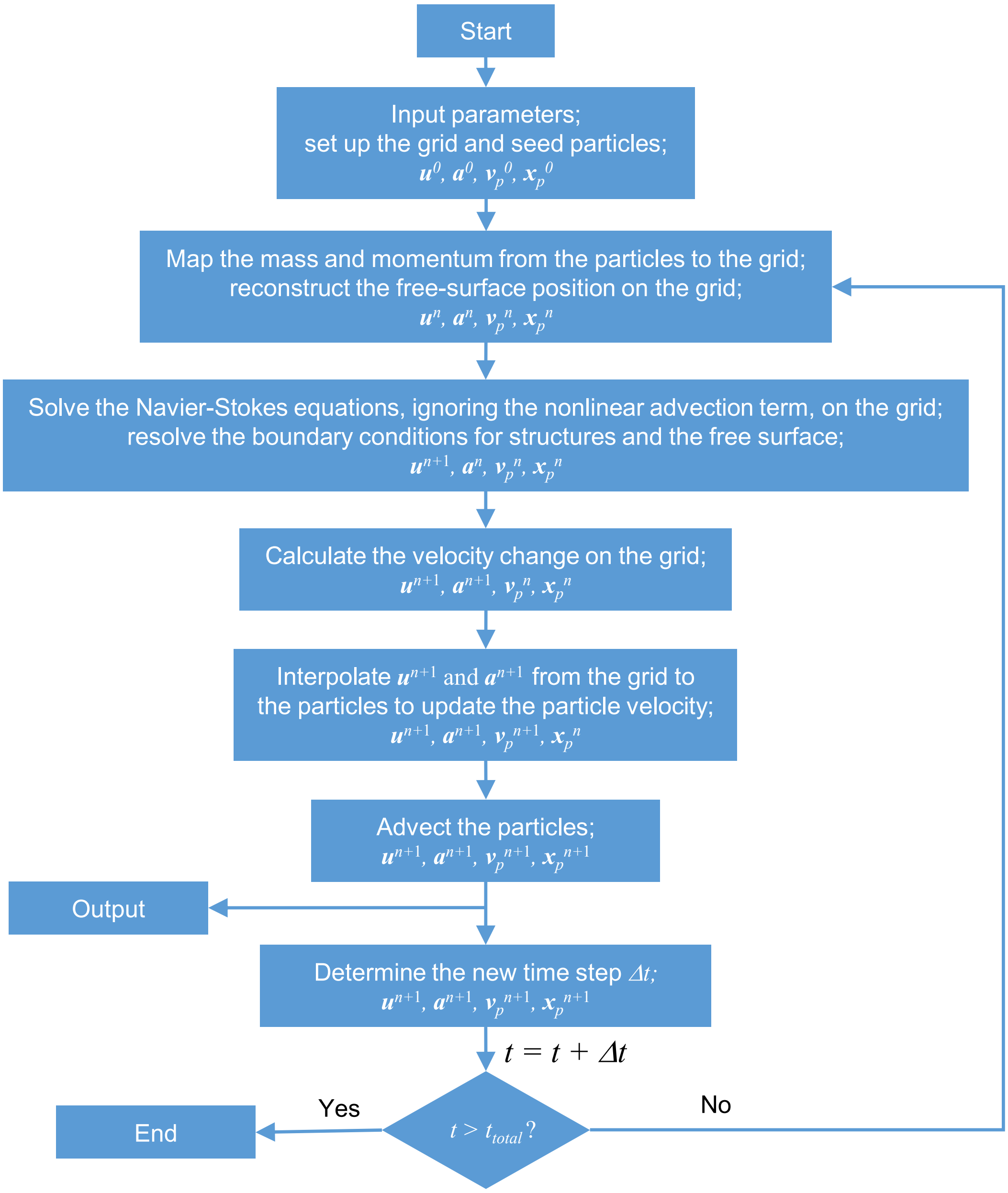

Fig. 3: A schematic showing the general algorithm of the PIC model. $\boldsymbol{u}$ and $\boldsymbol{a}$ are the velocity and the velocity change on the grid, $\boldsymbol{v}_p$ and $\boldsymbol{x}_p$ are the particle velocity and particle position, and n denotes the time level. $\boldsymbol{a}^{n+1} = \boldsymbol{u}^{n+1} - \boldsymbol{u}^n$.

floating breakwater so as to obtain more wave energy extraction but less wave transmission at the same time.

3.1. *Experimental setup*

The experiment of Ning et al. [6] was conducted in a wave flume at the State Key Laboratory of Coastal and Offshore Engineering, Dalian University of Technology, China. A piston-type unidirectional wavemaker is installed at one end of the flume, and a wave-absorbing beach is located at the other end to reduce the wave reflection. Fig. 4 shows a sketch depicting the setup of the physical model. The integrated system consisted of a vertical pile-restrained floating breakwater and a PTO system installed above the breakwater without changing the structure of the breakwater. The breakwater was restricted to heave motion only under wave action. Pulleys were used to connect the floating breakwater and the vertical pile. The friction coefficient between the pulley and the slide rail was 0.035 (determined by a friction coefficient measurement test). Note that the dimensions of the cross-section of the vertical pile were sufficiently small so that their influence on the wave field can be neglected. The heave motion of the breakwater was converted to the rotary motion of the shaft in the PTO system through the meshing engagement of a toothed rack on the connecting rod and a gear fixed at one end of the shaft (see Fig. 4). A current controller-magnetic powder brake system, which can produce approximate Coulomb damping force [6], and a torque-power sensor, which was used to measure the torque on the shaft, were connected to the other end of the shaft to simulate the power generation system (see Fig. 4). The PTO damping force was set by adjusting the input excitation current by the current controller. Four wave gauges were used to measure the free surface elevations as the experiment progressed; their locations are indicated in Fig. 4. The breakwater was a rectangular box measuring 0.8 m wide (B), 0.6 m high and 0.78 m long (D) in the transverse direction, with the gap between the breakwater and the flume wall being 0.01 m. The water depth h was fixed at 1.0 m, while the draft of the breakwater changed according to the test cases under consideration. Only regular waves were tested in the experiment and the test conditions are given in the following section. For more details about the experimental setup, the reader is referred to Ning et al. [6].

3.2. *Numerical setup*

In the present work, a 2D numerical wave tank (NWT) is established following Chen et al. [21]. Waves are generated in the x-direction using a piston-type wave paddle, which is installed at one end of the NWT (in the x-direction). At the other end, a relaxation zone is employed for wave absorption. The velocities of any particles that have entered the relaxation zone are gradually damped out. We note that in order to save on CPU cost, the length of the NWT was modified for different wave conditions. For example, a short

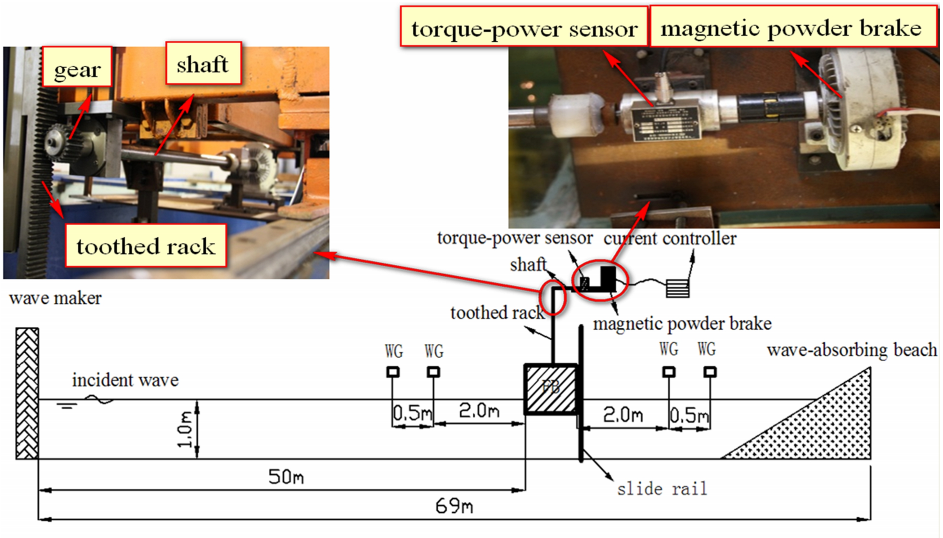

Fig. 4: A sketch of the experimental setup. WG: wave gauge. This figure is reprinted from Ning et al. [6], Copyright (2016), with permission from Elsevier.

NWT was used when the incident regular wave has a short wavelength. However, the floating breakwater was always placed at a position approximately 6 wavelengths away from the wave paddle to ensure that the motion of the floating breakwater is fully developed to a steady state before being contaminated by the re-reflected waves from the wavemaker. Having a shorter computational domain is also beneficial in terms of minimising any unwanted numerical diffusion that may be present. The length of the relaxation zone was kept at least 2 wavelengths long for each test condition in order to achieve the most cost-effective performance of wave absorption in the current PIC model [19].

The grid sizes were chosen as $\Delta x = \Delta z = 0.02$ m according to a grid convergence study, which is given in Section 3.4.1. The time step was controlled by the Courant number that was set to 0.5 for all the test cases.

In the numerical modelling, the PTO damping force $\boldsymbol{F}_{PTO}$ directly applied on the floating breakwater was in a standard Coulomb form as demonstrated in Fig. 5. The magnitude F of $\boldsymbol{F}_{PTO}$ was controlled by the input excitation current I, and their relations are given in Section 3.3. Note that the PTO damping force was always in the opposite direction of the heave motion of the floating breakwater. Another external force due to the friction between the pulleys and the slide rail was applied in the same manner, except that the magnitude of the friction force was determined by $\mu F_h(t)$, where μ is the friction coefficient and $F_h(t)$ is the horizontal wave force on the breakwater at time t.

In the physical experiment, the captured energy by the PTO system was analysed using

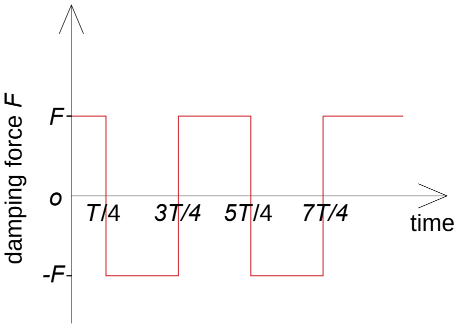

Fig. 5: A sketch showing the standard Coulomb damping force applied on the floating breakwater in the numerical simulation. F is the magnitude of the damping force and T is the wave period.

the power curve measured by the torque-power sensor that was installed between the shaft and the magnetic powder brake. In the numerical model, this is calculated equivalently using the PTO damping force:

$$P_c = 4F\delta/T\,, \tag{5}$$

where P_c is the captured wave power; F is the magnitude of the PTO damping force; δ is the amplitude of the heave motion of the floating breakwater and T is the wave period. The incident wave power is calculated by:

$$P_i = \frac{1}{16}\frac{\rho g H_i^2 \omega D}{k}\left(1+\frac{2hk}{\sinh 2hk}\right)\,, \tag{6}$$

where h is the water depth; k is the wave number; H_i is the incident wave height; ω is the wave frequency and D is the transverse length of the floating breakwater. Consequently, the CWR coefficient $\eta = P_c/P_i$.

The wave transmission coefficient K_t in the numerical model is calculated as H_t/H_i, where H_i is the incident wave height and H_t is the transmission wave height. The transmission wave height is calculated using the steady-state free-surface elevation extracted at the location of the first wave gauge behind the floating breakwater (see Fig. 4). It is noted that for all of the test cases, the transmission wave heights are all calculated using this wave gauge, which ensures consistency for obtaining the characteristic trend of the wave transmission coefficient.

3.3. Test conditions

Regular waves were used in the experiment. The test conditions of the selected test cases for validating the numerical model and the optimisation study are all given in Table 1, where

Table 1: Parameters of the test cases.

Test case	d (m)	T (s)	B/L	floating breakwater	Test type
1	0.20	1.16, 1.37, 1.58, 1.79, 2.00, 2.42	0.38, 0.28, 0.22, 0.18, 0.15, 0.12	Box	Validation
2	0.25	1.37, 1.58	0.28, 0.22	Box	Validation
3	0.25, 0.27, 0.30	1.37	0.28	Box	Validation
4	0.25	1.37, 1.58	0.28, 0.22	Models 1, 2, 3	Optimisation
5	0.25, 0.27, 0.30	1.37	0.28	Models 1, 2, 3	Optimisation
6	0.25	1.37, 1.58	0.28, 0.22	Models 4, 5	Optimisation

d is the draft of the floating breakwater, T is the wave period and L is the wavelength. Test cases 1-3 are validation cases, where experimental data are available for comparison and the floating breakwater is the rectangular box. Test cases 4 and 5 are optimisation study cases, where models 1-5 represent the modified breakwaters, whose shapes are sketched in Fig. 6. As shown in Fig. 6, models 1-3 have curve corners for both the seaward and the leeward sides, with their radii R ranging from 0.1 m to 0.4 m (full curve). Furthermore, models 4 and 5 are asymmetric and have one curve corner ($R = 0.1$ m) and one straight corner (as the rectangular box). In particular, while model 4 has a seaward side curve corner, model 5 has a leeward side curve corner.

For the validation cases, test case 1 considers one draft and six different incident wave periods, and the excitation current was kept constant to $I = 0.0$, i.e. no PTO damping force. With the inclusion of the PTO system, test case 2 looks into the effect of incident wave period on the hydrodynamic performance of the integrated system, and test case 3 focuses on the effect of the draft of the floating breakwater. Note that as the draft of the floating breakwater increases, the mass of the breakwater increases. For the optimisation study, the test conditions are all kept the same as those in the validation cases according to the test cases under consideration, with only different breakwaters as given in Fig. 6.

For each test case, the magnitudes of the PTO damping forces corresponding to the input excitation currents are digitised from Ning et al. [6] and given in Table 2. For all the test cases, the incident wave height H_i was fixed at 0.2 m.

3.4. Validation results and discussions

In this section, the numerical results from the present PIC model are compared with those from the experiment of Ning et al. [6]. Prior to that, a grid convergence study based on a free decay test is conducted to determine the grid size, and the capability of the present numerical model on predicting wave forces are also tested. For the latter, as no experimental data are available from Ning et al. [6], the experiment presented in Rodrguez and Spinneken

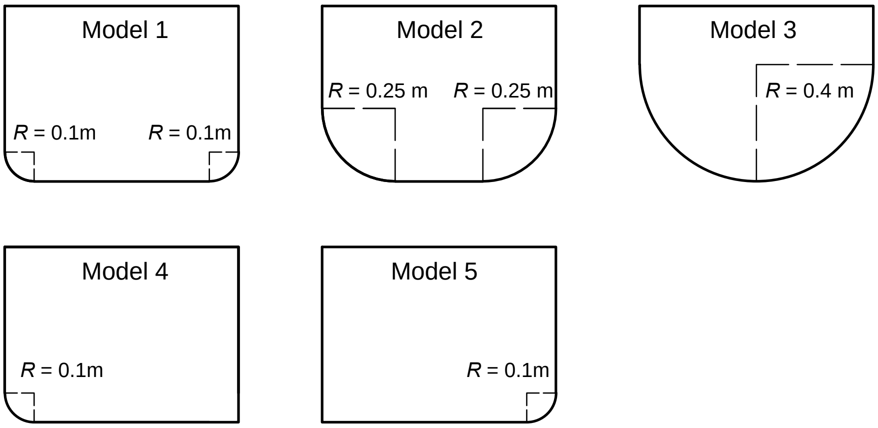

Fig. 6: Sketch showing the shapes of the designed breakwaters for the optimisation study. R is the radius of the curve corner.

Table 2: Magnitude of the PTO damping force for different test cases.

Test case	d (m)	T (s)	Excitation current I (A)	F (N)
1	0.20	the same as Table 1	0.00	0.00
2	0.25	1.37	0.06, 0.12, 0.18, 0.24, 0.30	13.85, 44.68, 80.00, 115.67, 130.91
	0.25	1.58	0.06, 0.12, 0.18, 0.24, 0.30	17.96, 43.00, 84.60, 121.21, 142.96
3	0.25	1.37	0.06, 0.12, 0.18, 0.24, 0.30	the same as Test case 2
	0.27	1.37	0.06, 0.12, 0.18, 0.24, 0.30	19.75, 52.66, 77.22, 107.34, 134.68
	0.30	1.37	0.06, 0.12, 0.18, 0.24, 0.30	15.44, 47.34, 87.59, 118.48, 130.13
4	0.25	1.37, 1.58	0.06, 0.12, 0.18, 0.24, 0.30	the same as Test case 2
5	0.25,0.27,0.30	1.37	0.06, 0.12, 0.18, 0.24, 0.30	the same as Test case 3
6	0.25	1.37,1.58	0.06, 0.12, 0.18, 0.24, 0.30	the same as Test case 2

[22] are adopted, where both the wave and structure characteristics are similar to those used in Ning et al. [6] and experimental data regarding wave forces are available.

3.4.1. Grid convergence study

Grid convergence studies were carried out to determine the grid size for the current numerical simulations. These were based on the free decay tests of the heave motion of the floating breakwater for the rectangular box and Model 2 (see Fig. 6). Initially, the floating breakwater had a draft of 0.25 m and no PTO damping force was considered. The floating breakwater was then lifted up by approximately 0.24 m and released, resulting in a free motion of vertical oscillation. Three different grid sizes were used for the tests; they were $\Delta x = \Delta z = B/20$ (the coarse grid), $B/40$ (the moderate grid) and $B/80$ (the fine grid), where $B = 0.8$ m is the width of the floating breakwater. Fig. 7 shows the results for the three grid sizes. In particular, for the rectangular box case, the experimental data are also available for comparison. In terms of the convergence study, it may be seen from Fig. 7 that for both floating breakwater shapes the heave motion produced by the moderate grid tends to have a smaller discrepancy than that by the coarse grid, when compared with the result by the fine grid. Using the result of the fine grid as reference and taking 80 points equally across the time range from 0.056 s to 4.006 s, the root mean square errors (RMSE) of the results by the moderate and the coarse grid are 0.00295 and 0.00505 for the rectangular box case and 0.00139 and 0.00289 for Model 2 case (see Fig. 6), respectively. Both data pairs show that the results are converging. Note that because the present PIC model uses a double-grid system (i.e. grid and particles), the memory storage requirement is very demanding for the fine grid case. Considering that the results by the moderate grid are very close to those of the fine grid, the moderate grid ($\Delta x = \Delta z = B/40$) is finally chosen for the numerical simulations.

Regarding the comparison between the numerical and experimental results for the rectangular box case, it can be seen that the experimental data show a longer natural period and larger damping of the integrated system. This is due to the fact that the effect of the rotary motion of the shaft in the PTO system (see Fig. 4) is neglected in the numerical simulations, which is because of a lack of dimension and weight information for the shaft from the experiment. The shaft in fact adds to the overall mass of the integrated system and hence increases its natural period. Moreover, the frictions in the experiment due to the transmission mechanism are also ignored in the numerical simulation; this contributes to the larger damping as seen in the experimental data.

3.4.2. Wave force validation

The capability of the present numerical model on predicting the wave force on structures is investigated in this section. As such experimental data is not available from Ning et al. [6], the experiment proposed in Rodrguez and Spinneken [22] was used. In the latter experiment, a 2D rectangular box with a draft of b and a width of $2b$ was fixed approximately in the centre of a wave flume. The water depth was fixed at $h = 5b$. Regular waves were generated to interact with the box and the vertical excitation wave forces on the box were measured. Two test cases were selected for the current validation: (a) $kb = 0.4$ and (b) $kb = 0.7$, where k is the wave number. In both cases, the wave steepness kA_I (A_I is the incident wave amplitude) was 0.10. For full details of the experimental setup, the reader is refer to Rodrguez and Spinneken [22].

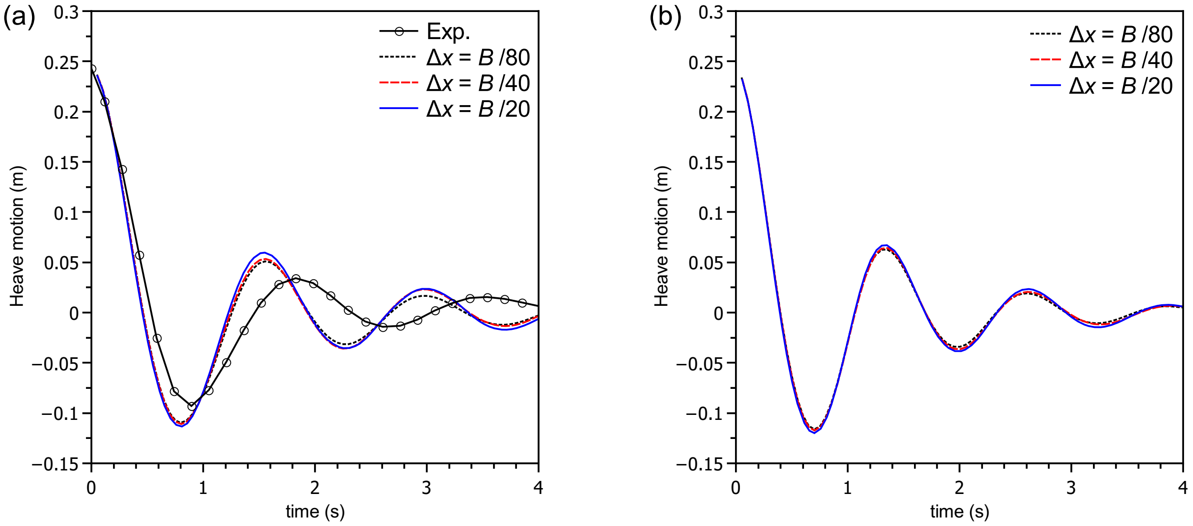

Fig. 7: Grid convergence study on the free decay test of the heave motion of the floating breakwater for (a) rectangular box and (b) box with curve corners (Model 2, see Fig. 6).

Fig. 8 presents the comparison of the non-dimensionalised vertical wave force $F(t)/\rho g A_I b$ (per unit length in the transverse direction) between the present numerical results and the experimental data. From the asymmetric vertical wave force it is shown that strong nonlinearities are involved in both test cases, particularly for $kb = 0.7$. In general, the agreement between the numerical and experimental results is satisfying, which demonstrates the capability of the present numerical model in terms of wave force prediction.

3.4.3. Validation of the WEC-type floating breakwater simulation

This section concerns the validation of the present numerical model on modelling the hydrodynamic performance of the integrated WEC-type floating breakwater proposed in Ning et al. [6]. These correspond to the test cases 1-3 listed in Table 1.

Test case 1 concerns the effect of incident wave frequency and no PTO damping force was applied. Fig. 9 shows the comparison between numerical and experimental results for the non-dimensionalised heave motion response of the floating breakwater, ξ/H_i, for various incident wave periods. In general, it is seen that the numerical results match well with the experimental data. Nevertheless, it may be also seen that the overall numerical curve shifts slightly to higher relative wave frequencies (i.e. B/L) than the experimental curve. This is likely due to the fact that the shaft in the PTO system (see Fig. 4) is not simulated in the numerical model. As discussed in Section 3.4.1, the shaft in theory increases the overall mass of the integrated system and hence lowers its natural frequency.

Test case 2 considers two incident wave periods $T = 1.37$ s and 1.58 s (i.e. $B/L =$

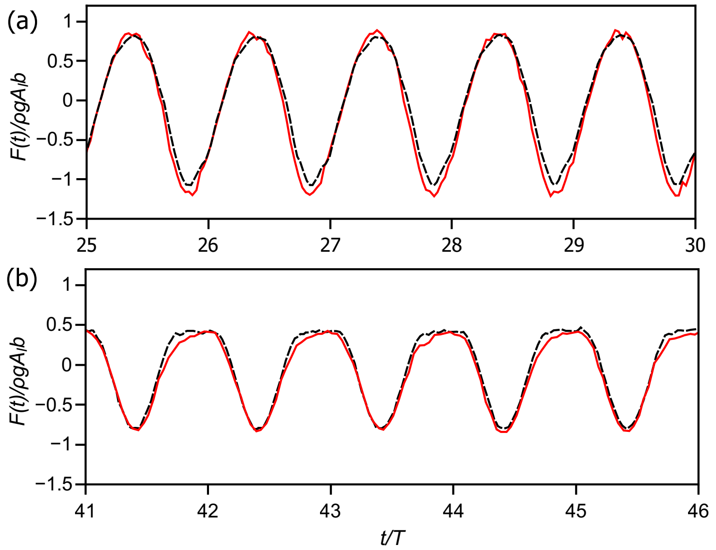

Fig. 8: Comparison of the time-history of the vertical excitation force due to regular waves with $kA_I = 0.10$, and (a) $kb = 0.4$ and (b) $kb = 0.7$. Solid line: present numerical result; dashed line: experimental data digitised from Rodrguez and Spinneken [22].

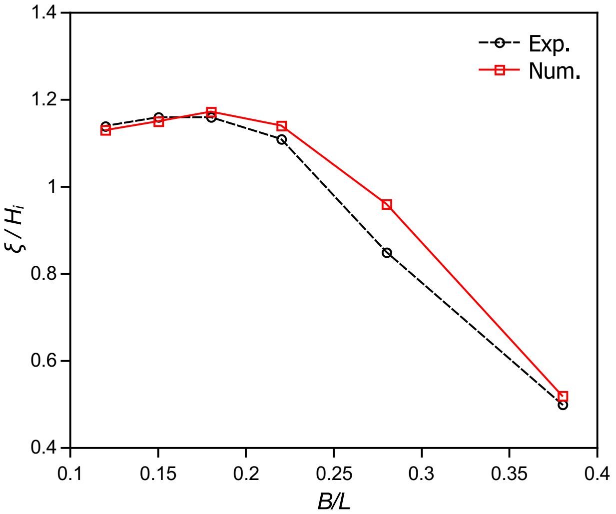

Fig. 9: Comparison of the heave motion response of the floating breakwater for various incident wave periods.

0.28 and 0.22) and in both scenarios the PTO damping force was applied, whose magnitude was determined by the excitation current (see Table 2). Fig. 10 plots the comparisons for the non-dimensional heave response of the floating breakwater ξ/H_i, the CWR coefficient η and the transmission coefficient K_t all as a function of the excitation current. From Fig. 10(a) it is seen that for both wave periods the magnitude of the heave response of the floating breakwater decreases as the PTO damping force increases. The numerical results

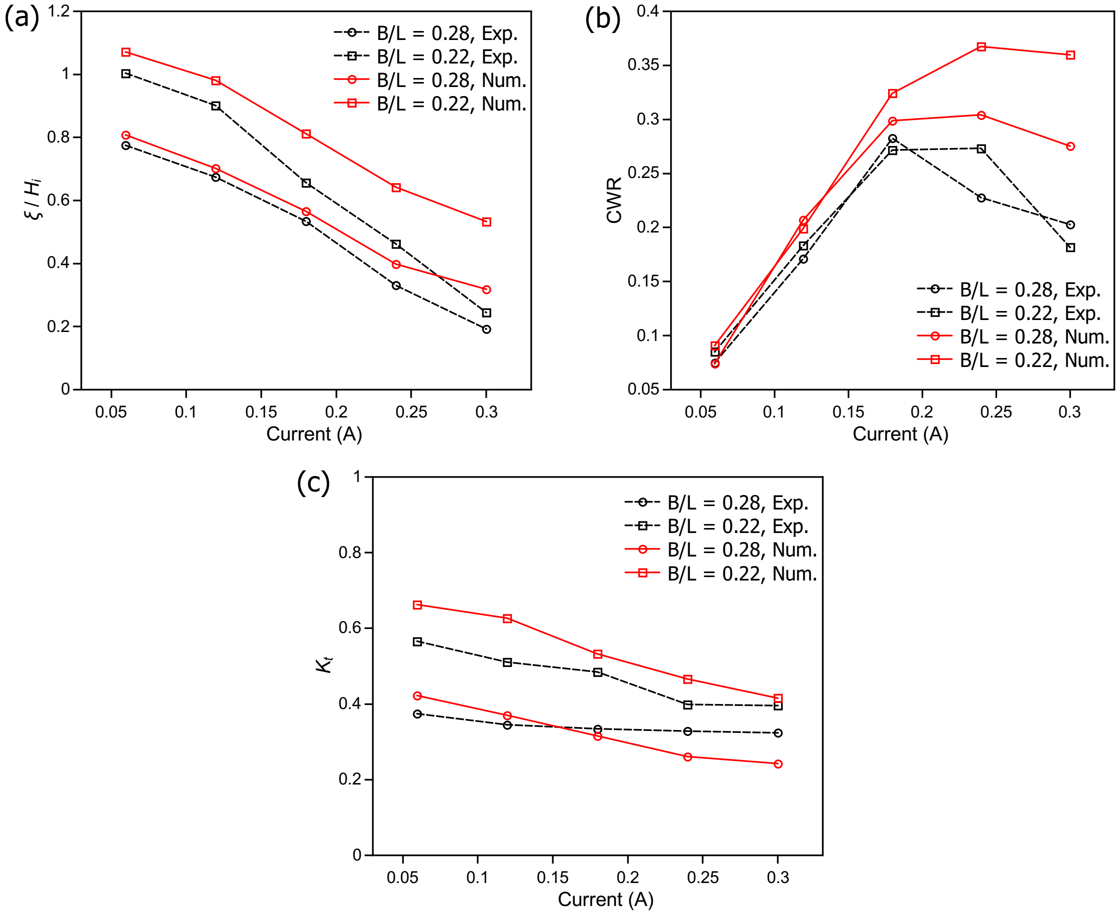

Fig. 10: Comparisons between numerical and experimental results for (a) non-dimensional heave response ξ/H_i, (b) CWR η and (c) transmission coefficient K_t.

are in general greater than the experimental data, which can be explained by the additional friction forces caused in the experiment as well as the above-mentioned effect of neglecting the motion of the shaft in the numerical model. Moving to Fig. 10(b), it is seen that generally the numerical predictions of the CWR coefficients are greater than the experiment due to the larger heave motion responses. However, the numerical model well predicts the ranges where optimal peaks of the CWR coefficient occur. Fig. 10(c) shows the comparison for the transmission coefficient; it is seen that wave transmission decreases as the heave motion of the breakwater decreases (see Fig. 10(a)) and the longer wave period leads to larger wave transmission as expected [23]. It is interesting to see that the optimal peak of the CWR coefficient occurs in the range where the wave transmission coefficient is low, which demonstrates the feasibility of such integrated system with regard to both wave energy absorption and wave attenuation.

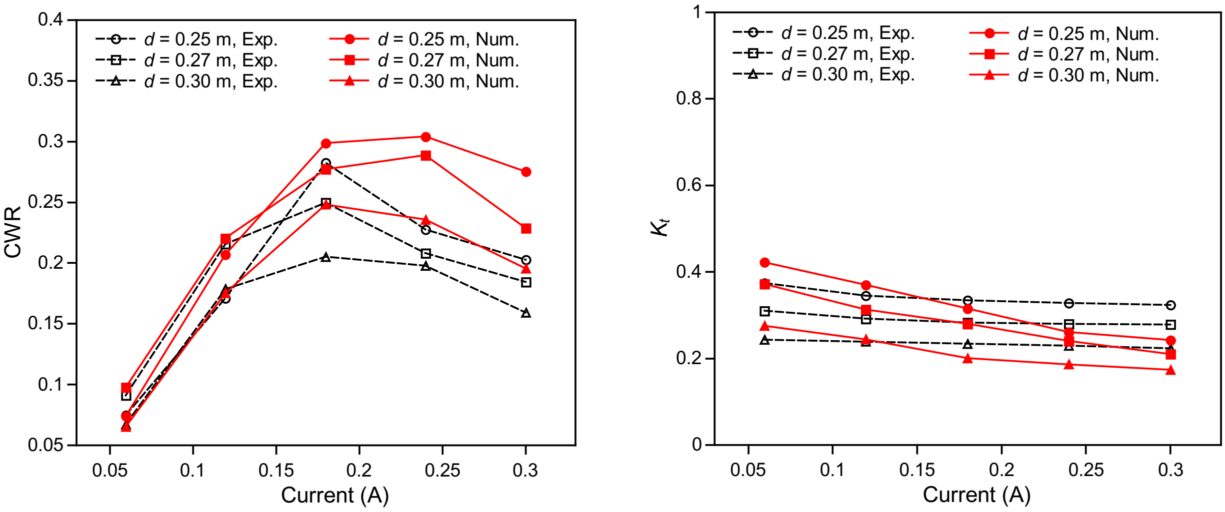

Fig. 11: Comparisons between numerical results and experimental measurements for the CWR coefficient η (left panel) and wave transmission coefficient K_t (right panel). The results are for $T = 1.37$ s.

In test case 3, the effect of the draft of the floating breakwater is investigated. Fig. 11 presents the comparisons for the CWR coefficient and the wave transmission coefficient. It can be seen that in general the numerical results match reasonably well with the experimental data for both the CWR and wave transmission coefficients. The larger draft d leads to smaller magnitude of the heave response of the floating breakwater as it becomes heavier and hence smaller CWR coefficients. The larger draft d also leads to smaller wave transmission coefficient. These results are consistent with the findings by Isaacson et al. [23].

In short summary, the above comparisons demonstrate that the present PIC model is capable of well predicting the key physical processes occurring in these validation test cases. Based on that, the optimisation study were conducted and the results are discussed in the following sections.

3.5. Optimisation study

The optimisation study in this section aims to further understand the performance of the integrated system in the above experiment via changing the shape of the floating breakwater, and to provide guidance for designation of a better floating breakwater to achieve high CWR but low wave transmission at the same time.

3.5.1. Symmetric structure with curve corners

Test cases 4 and 5 consider the symmetric models 1-3 with curve corners (see Fig. 6) as alternative floating breakwaters and all the other settings, such as the PTO damping force,

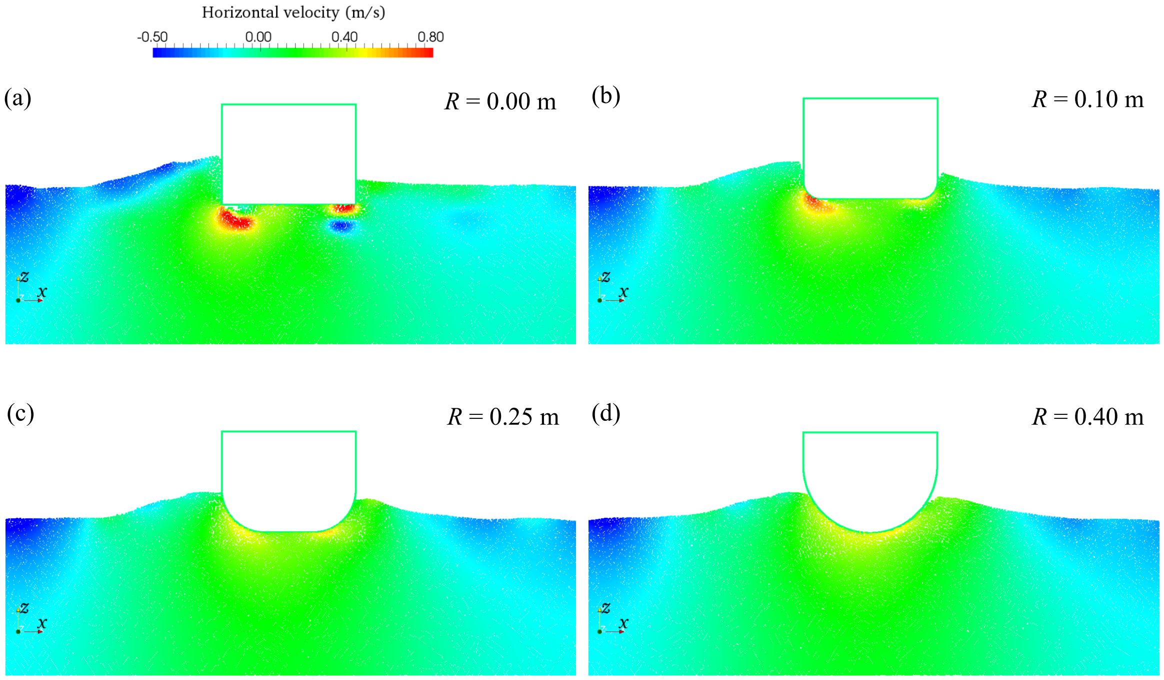

Fig. 12: Snapshot of the numerical results for different floating breakwaters at similar time instants. The test conditions are $T = 1.58$ s, $I = 0.06$ A and $d = 0.25$ m.

are set the same as those used in test cases 2 and 3, respectively.

Fig. 12 shows the snapshot of the numerical results run by using different floating breakwaters. It is seen that by changing the straight corners to curve corners, the velocity gradient of the fluid field around the corners becomes smaller as the radii of the corners increase. Also, it seems that the wave can move past the breakwater more easily when the radii of the corners increase.

For test case 4, Fig. 13 presents the numerical results of the CWR coefficient and the wave transmission coefficient for various symmetric floating breakwaters (models 1-3, see Fig. 6). From the CWR coefficient plots, it is seen that the floating breakwaters with curve corners ($R > 0.0$ m) generally perform better than the rectangular box ($R = 0.0$ m), in terms of wave energy extraction. This is likely due to that much less vortices were generated around the corners when curve corners were used (see Fig. 12) and hence a much smaller eddy making damping was induced. In particular, for the case when $T = 1.37$ s ($B/L = 0.28$), the optimal CWR coefficient is increased by approximately 40%. This significant increase may be also due to that $T = 1.37$ s is close to the natural periods of the floating breakwaters with curve corners, which range from approximately 1.43 s to 1.18 s as the radii

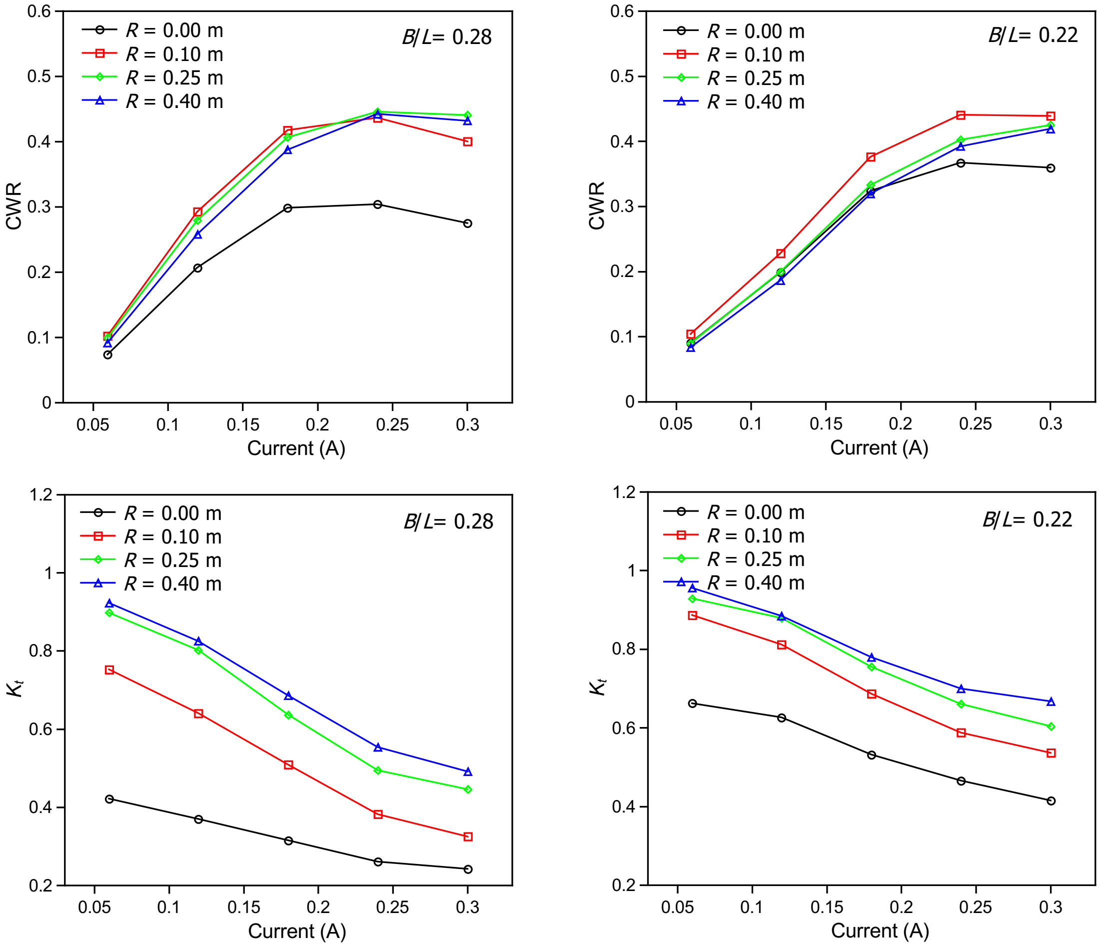

Fig. 13: Numerical results of the CWR coefficient (upper panels) and wave transmission coefficient K_t (lower panels) for symmetric floating breakwaters with various radii of the corners. The draft $d = 0.25$ m for all cases.

of the corners increase from 0.10 m to 0.40 m according to a number of free decay tests in the numerical model. On the other hand, from the results of the wave transmission coefficient, it is seen straightforwardly that as the radii of the structure corners increase, the wave transmission coefficient increases as well. The original rectangular box achieves the best performance from this point of view. Nevertheless, it is observed that the breakwater with the smallest curve corners, i.e. model 1 ($R = 0.10$ m), also leads to small wave transmission coefficients that are close to those of the rectangular box, particularly in the ranges where the optimal CWR occurs. Therefore, considering the outstanding performance on wave energy extraction, model 1 with small curve corners may prove to be an optimised design for the floating breakwater in such integrated system.

Test case 5 considers the effect of the draft on the performance of the integrated system

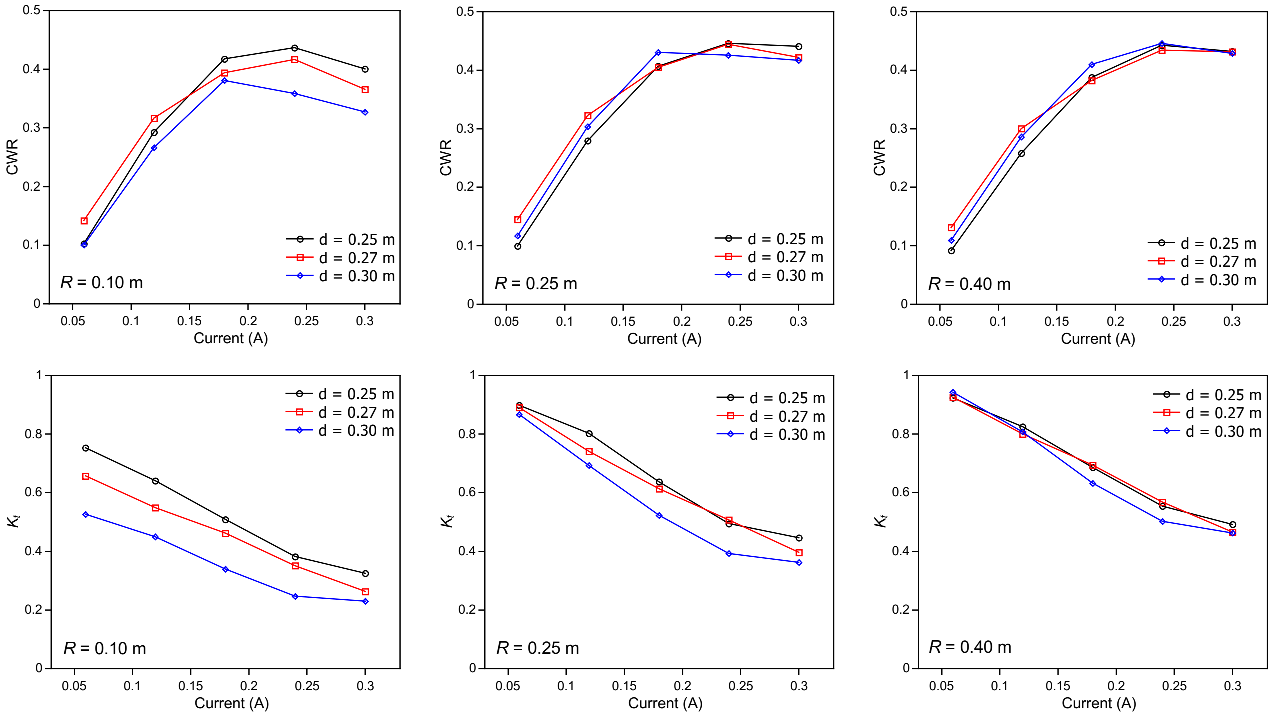

Fig. 14: Numerical results of the CWR coefficient (upper panels) and wave transmission coefficient K_t (lower panels) for symmetric floating breakwaters subjected to three different drafts. The wave period is 1.37 s.

when models 1-3 (see Fig. 6) are used as the floating breakwater. Fig. 14 plots the numerical results for both the CWR and wave transmission coefficients for models 1-3 all subjected to three different drafts. It can be seen from Fig. 14 that the influence of the draft on the performance of the integrated system reduces as the radii of the curve corners increase. While the small curve breakwater case ($R = 0.10$ m) shows a similar effect of the draft to that in the rectangular box case (see Fig. 11), the full curve breakwater case ($R = 0.40$ m) illustrates that the draft has a very weak effect on the performance of the integrated system. This more or less demonstrates that the floating breakwater with small curve corners has more flexibilities than those with large curve corners.

3.5.2. Asymmetric structure with curve and straight corners

The test cases presented above show that the performance of the integrated WEC-type floating breakwater can be optimised by modifying the straight corners of the floating breakwater to small curve corners. It may be also concluded that the curve corners result in large CWR due to a reduction of the eddy making damping but also large wave transmission as waves can move past the curve corners more easily, while the straight corners do the opposite. So, it may be interesting to see the results of a floating breakwater with both a curve and a straight corner. Test case 6 investigates the performance of the asymmetric models 4 and 5 (see Fig. 6), which have only one small curve corner ($R = 0.10$ m) in the seaward side and in the leeward side, respectively. The other test conditions are set the same as those used in test case 2.

Fig. 15 presents the results of the CWR and wave transmission coefficients for the asymmetric models 4 and 5, in comparison with those of the rectangular box and the symmetric model 1 ($R = 0.10$ m). It can be seen that in general model 4 achieves a similar performance to model 1 in terms of the CWR coefficient, but with the wave transmission coefficient being further reduced. On the other hand, model 5 produces CWR coefficients close to those by the rectangular box, but with larger wave transmission coefficients. The reason behind this is likely to be that the wave height in the seaward side is larger than that in the leeward side and hence the eddy making damping around the seaward side corner of the rectangular box is predominant; by modifying the seaward side straight corner to a small curve corner, the major eddy making damping is significantly reduced and hence larger CWR coefficients were achieved. Furthermore, keeping the leeward side straight corner can more or less help reduce wave transmission as discussed above. These lead to the conclusion that model 4 is a further optimisation of the small curve model 1, while model 5 is not recommended.

4. Conclusions

This paper presents a numerical study of the hydrodynamic performance of a vertical pile-restrained WEC-type floating breakwater, which is experimentally investigated in Ning et al. [6]. The numerical model solves the incompressible Navier-Stokes equations for free-surface flows using the PIC method, and incorporates a Cartesian cut cell based two-way strong coupling algorithm for fluid-structure interaction. The numerical model is first validated against the experimental measurements and then used for an optimisation study. The validation results show that the PIC model can well capture the key physical processes occurring in this complex wave-structure interaction scenario. Regarding the optimisation study, the results show that by modifying only the seaward side straight corner of the rectangular box floating breakwater proposed in Ning et al. [6] to a small curve corner, the integrated system achieves significantly more wave energy extraction at the cost of only a slight increase in wave transmission. For further research, a new physical experiment based on the optimised shape of the floating breakwater is under consideration.

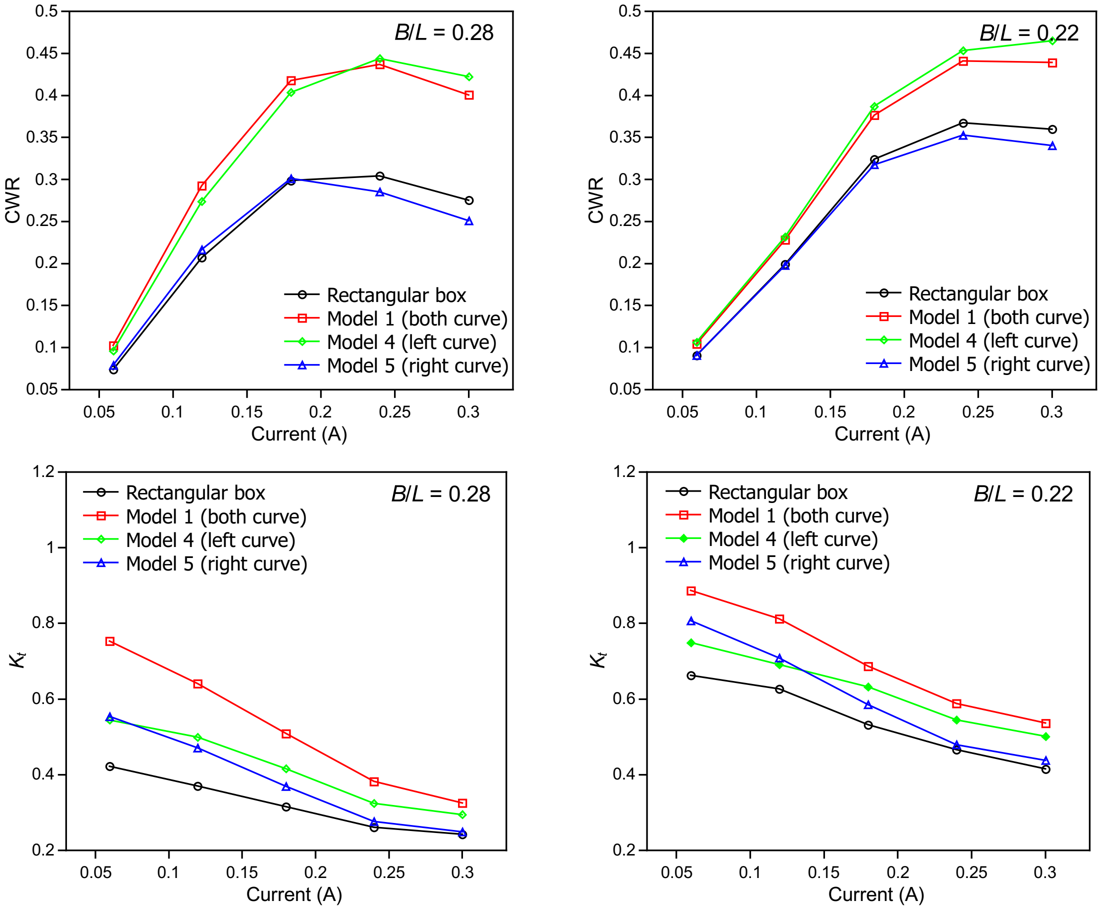

Fig. 15: Numerical results of the CWR coefficient (upper panels) and wave transmission coefficient K_t (lower panels) for asymmetric base models 4 and 5, in comparison with those by the rectangular box and model 1.

Acknowledgements

This work is supported by the UK Engineering and Physical Sciences Research Council (EPSRC) (Grant No. EP/R007519/1), the Open Funding of the State Key Laboratory of Coastal and Offshore Engineering at Dalian University of Technology (Grant No. LP1803) and the Royal Academy of Engineering (RAE) (Grant No. UK-CIAPP/73).

References

[1] J. Dai, C. M. Wang, T. Utsunomiya, W. Duan, Review of recent research and developments on floating breakwaters, Ocean Engineering 158 (2018) 132 – 151.

[2] A. G. L. Borthwick, Marine renewable energy seascape, Engineering 2 (2016) 69 – 78.

[3] M. A. Mustapa, O. B. Yaakob, Y. M. Ahmed, C.-K. Rheem, K. K. Koh, F. A. Adnan, Wave energy

device and breakwater integration: A review, Renewable and Sustainable Energy Reviews 77 (2017) 43 – 58.

[4] C. Michailides, D. C. Angelides, Modeling of energy extraction and behavior of a Flexible Floating Breakwater, Applied Ocean Research 35 (2012) 77 – 94.

[5] F. He, Z. Huang, A. W.-K. Law, An experimental study of a floating breakwater with asymmetric pneumatic chambers for wave energy extraction, Applied Energy 106 (2013) 222 – 231.

[6] D. Ning, X. Zhao, M. Gteman, H. Kang, Hydrodynamic performance of a pile-restrained WEC-type floating breakwater: An experimental study, Renewable Energy 95 (2016) 531 – 541.

[7] F. H. Harlow, A Machine Calculation Method for Hydrodynamic Problems, Technical Report LAMS-1956, Los Alamos Scientific Laboratory, Los Alamos, 1955.

[8] F. H. Harlow, The Particle–In–Cell computing method for fluid dynamics, in: B. Alder (Ed.), Methods in Computational Physics, Academic Press, New York, 1964, pp. 319–343.

[9] F. H. Harlow, Fluid dynamics in Group T-3 Los Alamos National Laboratory: (LA-UR-03-3852), Journal of Computational Physics 195 (2004) 414 – 433.

[10] J. U. Brackbill, H. M. Ruppel, FLIP: A method for adaptively zoned, Particle-In-Cell calculations of fluid flows in two dimensions, J. Comp. Phys. 65 (1986) 314–343.

[11] J. U. Brackbill, D. B. Kothe, H. M. Ruppel, FLIP: A low-dissipation, Particle-In-Cell method for fluid flow, Computer Physics Communications 48 (1988) 25–38.

[12] E. Edwards, R. Bridson, A high-order accurate Particle–In–Cell method, International Journal for Numerical Methods in Engineering 90 (2012) 1073–1088.

[13] J. M. Maljaars, R. J. Labeur, M. Möller, A hybridized discontinuous galerkin framework for high-order particlemesh operator splitting of the incompressible navierstokes equations, Journal of Computational Physics 358 (2018) 150 – 172.

[14] W. Wang, D. M. Kelly, A high-order PIC method for advection-dominated flow with application to shallow water waves, International Journal for Numerical Methods in Fluids 87 (2018) 583–600.

[15] D. M. Kelly, Full particle PIC modelling of the surf and swash zones, in: Proc. 33rd Int. Conf. Coast. Eng., A.S.C.E., Santander, 2012, pp. 77–92.

[16] D. M. Kelly, Q. Chen, J. Zang, PICIN: A Particle–In–Cell solver for incompressible free surface flows with two-way fluid-solid coupling, SIAM Journal on Scientific Computing 37 (2015) B403–B424.

[17] Q. Chen, J. Zang, A. S. Dimakopoulos, D. M. Kelly, C. J. Williams, A Cartesian cut cell based two-way strong fluid-solid coupling algorithm for 2D floating bodies, Journal of Fluids and Structures 62 (2016) 252 – 271.

[18] Q. Chen, J. Zang, D. M. Kelly, A. S. Dimakopoulos, A 3D parallel particle-in-cell solver for wave interaction with vertical cylinders, Ocean Engineering 147 (2018) 165 – 180.

[19] Q. Chen, Development of A Full Particle PIC Method for Simulating Nonlinear Wave-Structure Interaction, Ph.D. thesis, University of Bath, 2017.

[20] A. J. Chorin, Numerical solution of the Navier–Stokes equations, Math. Comput. 22 (1968) 745–762.

[21] Q. Chen, D. M. Kelly, A. S. Dimakopoulos, J. Zang, Validation of the PICIN solver for 2D coastal flows, Coastal Engineering 112 (2016) 87 – 98.

[22] M. Rodrguez, J. Spinneken, A laboratory study on the loading and motion of a heaving box, Journal of Fluids and Structures 64 (2016) 107 – 126.

[23] M. Isaacson, J. Baldwin, S. Bhat, Wave propagation past a pile-restrained floating breakwater, International Journal of Offshore and Polar Engineering 8 (1998) 265–269.